JOURNAL OF SYNCHROTRON RADIATION
ISSN 1600-5775

Comparative analysis of XANES and EXAFS for local structural characterization of disordered metal oxides

Junying Li,[a] Yuanyuan Li,[a] Prahlad K. Routh,[a] Evgeniy Makagon,[b] Igor Lubomirsky[b] and Anatoly I. Frenkel[a]*

[a]Materials Science and Chemical Engineering, Stony Brook University, 100 Nicolls Road, Stony Brook, NY 11794, USA, and [b]Department of Materials and Interfaces, Weizmann Institute of Science, Rehovot 7610001, Israel. *Correspondence e-mail: anatoly.frenkel@stonybrook.edu

Received 30 April 2021
Accepted 7 July 2021

Edited by S. M. Heald, Argonne National Laboratory, USA

Keywords: functional materials; XAFS; pre-edge analysis; local symmetry.

Supporting information: this article has supporting information at journals.iucr.org/s

In functional materials, the local environment around active species that may contain just a few nearest-neighboring atomic shells often changes in response to external conditions. Strong disorder in the local environment poses a challenge to commonly used extended X-ray absorption fine structure (EXAFS) analysis. Furthermore, the dilute concentrations of absorbing atoms, small sample size and the constraints of the experimental setup often limit the utility of EXAFS for structural analysis. X-ray absorption near-edge structure (XANES) has been established as a good alternative method to provide local electronic and geometric information of materials. The pre-edge region in the XANES spectra of metal compounds is a useful but relatively under-utilized resource of information of the chemical composition and structural disorder in nanomaterials. This study explores two examples of materials in which the transition metal environment is either relatively symmetric or strongly asymmetric. In the former case, EXAFS results agree with those obtained from the pre-edge XANES analysis, whereas in the latter case they are in a seeming contradiction. The two observations are reconciled by revisiting the limitations of EXAFS in the case of a strong, asymmetric bond length disorder, expected for mixed-valence oxides, and emphasize the utility of the pre-edge XANES analysis for detecting local heterogeneities in structural and compositional motifs.

1. Introduction

In functional materials, the local environment around various atomic species may change dynamically under different *operando* conditions, such as elevated temperature, pressure and application of external electric fields (Vaccari *et al.*, 2009; Dalba *et al.*, 2004). The local atomic displacements introduce distortions in the bond lengths, which affect specific functional properties such as piezoelectricity, ferroelectricity and pyroelectricity (Abrahams, 1978). A variety of experimental methods such as atomic scale microscopy, X-ray diffraction (XRD) and X-ray photoelectron spectroscopy (XPS) have been developed and utilized to study these changes (Ueda, 2013; Feldmann, 2003; Wang *et al.*, 2013). Nevertheless, the choice of tools for detecting and interpreting small structural changes in functional materials is limited. X-ray absorption spectroscopy (XAS) is a premier technique to probe the structure at the atomic scale (Rehr & Albers, 2000; Sayers *et al.*, 1971; Bingham *et al.*, 2014; Wende, 2004; Penner-Hahn, 1999; Grunes, 1983; Farges *et al.*, 2004; Sayers *et al.*, 1969; Ankudinov *et al.*, 2002; Frenkel *et al.*, 2001). In particular, extended X-ray absorption fine structure (EXAFS) provides essential information on the distribution of neighboring atoms

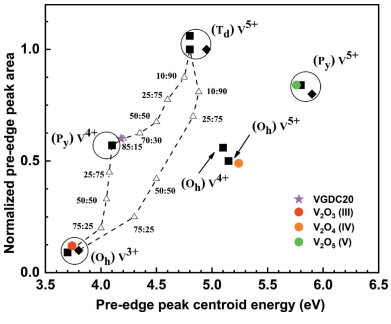

around the absorbing atom, which has excellent sensitivity to local atomic displacement and is element-specific. EXAFS analysis commonly assumes Gaussian distribution of bond lengths, which is usually sufficient to understand the local symmetry of well defined materials, such as homogeneous, single-phase bulk solids (Timoshenko *et al.*, 2019). However, interatomic distance distribution can be more complicated in many materials, such as metallic nanoparticles, mesoporous materials and metals in molten salts (Boubnov *et al.*, 2020; Prasai *et al.*, 2015; Billinge & Levin, 2007; McGreevy & Pusztai, 1990; Dias *et al.*, 2021), where the local atomic environment is characterized by strong asymmetry in the bond length distribution. Such an asymmetry has been shown to be a source of artifacts in conventional structural analysis methods by EXAFS (Yevick & Frenkel, 2010). In these cases, the non-Gaussian distribution of bond length needs to be accounted for in order to understand the local environment, which introduces the inaccuracy in quantitative analysis of experimental EXAFS spectra. The alternative approaches used to circumvent the limitations of conventional EXAFS analysis generate the theoretical EXAFS spectra based on atomic level simulations, *e.g.* molecular dynamics (MD) or reverse Monte Carlo simulations (RMC) methods (Chill *et al.*, 2015; Yancey *et al.*, 2013; Gurman & McGreevy, 1990). The quality of the agreement between theoretical and experimental EXAFS spectra can be used to determine the atomic structures. In the MD simulation method, the interatomic forces are derived from *ab initio* calculation or empirical force fields (Chill *et al.*, 2015; Cicco *et al.*, 2002 & Roscioni *et al.*, 2011). Although this approach can be employed to study the local structure by modeling thermal disorder and anharmonic effects, the MD simulation method is limited to simulations of the smaller clusters (1–2 nm in size) (Mazzone *et al.*, 2008). In RMC, the configuration-averaged EXAFS is calculated after the positions of the atoms in the assumed 3D structure model are randomly modified at each interaction, and then, the optimized structure is generated after minimizing the difference with the experimental and calculated EXAFS (McGreevy & Pusztai, 1988; Timoshenko & Frenkel, 2017).

X-ray absorption near edge structure (XANES) can be employed as a complementary method to EXAFS to obtain local electronic and geometric information because it is sensitive to the electronic transitions and the multiple-scattering contributions from neighboring atoms (Rehr *et al.*, 1992; Ankudinov *et al.*, 2002). Furthermore, the pre-edge features in the XANES spectra also contain information about the electronic and structural properties of materials (Srivastava & Nigam, 1973). The pre-edge features and the main-edge features of the experimental XANES spectra of some transition metals are well studied through understanding the features in theoretical XANES spectra, which are typically obtained by the so-called forward modeling approach (Rehr & Albers, 2000; Joly, 2001; Vinson *et al.*, 2011). For example, Farges *et al.* (1997) successfully modeled the Ti *K*-edge XANES spectra for selected Ti compounds using the *ab initio* real space multi-scattering approach (FEFF) to interpret the features of the experimental XANES spectra, including the pre-edge features and main-edge features, providing a quantitative description of the Ti *K*-edge XANES spectra. Farges *et al.* show that the shapes of the XANES spectra are affected by the size and the types of clusters around the Ti atoms. In addition, the characteristic pre-edge features associated with the coordination number (CN) of a central atom have been utilized as a powerful tool to help understand the local symmetry (Farges *et al.*, 1997). As explained by Farges *et al.*, for the Ti^{4+} species, the pre-edge energy position and pre-edge intensity are well separated for the different CNs. Other works discussed the pre-edge features according to group theory calculations and indicated that, although the oxidation states can be the same, the different types of symmetries, *e.g.* tetrahedral (T_d) and octahedral (O_h), affect the intensities of the pre-edge features differently (Yamamoto, 2008). More recent applications of the sensitivity of the pre-edge features to the local environment of metal oxides were used as a basis of the machine learning based approaches to predict the XANES spectra of metal oxides with quantitative accuracy (Liu *et al.*, 2019; Carbone *et al.*, 2020; Torrisi *et al.*, 2020).

In general, the results obtained by XANES such as charge states and local geometry are used to support the information extracted by EXAFS analysis, such as CNs. However, as for the materials with strong asymmetry in the bond length distribution, the results obtained by XANES and EXAFS could be inconsistent. In addition, for functional materials, dilute concentrations of absorbing atoms, low dimensionality of sample size and the experimental setup (*e.g.* reaction cell walls) pose obstacles toward collecting the experimental EXAFS spectrum with sufficient quality for adequate structural analysis. In these cases when EXAFS analysis is unavailable or unreliable, the pre-edge analysis stands out as the sole source of information on the local symmetry from X-ray absorption measurement.

In this study, we illustrate this problem – the inconsistency in the determination of the local environment by XANES and EXAFS when strongly asymmetric disorder in the bonding distribution is present – using an example of two different metal oxide nanocomposite materials, in which the local environment of the transition metal is either distorted octahedral, *i.e.* relatively symmetric, or strongly asymmetric. In the former case, EXAFS results agree with those obtained from the pre-edge analysis. In the latter case, they are inconsistent because conventional EXAFS is affected by the strong and asymmetric disorder. We focus on the Ti-doped $Ce_{0.8}Gd_{0.2}O_{1.9}$ (TiGDC20) and V-doped $Ce_{0.8}Gd_{0.2}O_{1.9}$ (VGDC20) nanocomposites, which are shown to have different local symmetries for transitional metal's environment (*vide infra*). In the case of the Ti environment, although there is a high disorder, the environment is a distorted octahedral. We demonstrate that, in this case, the EXAFS results and pre-edge analysis results are consistent. TiGDC20 composites were recently shown to have exceptionally high oxygen diffusion coefficients at room temperature ($\simeq 10^{-14}$ cm^2 s^{-1}) and reversible oxidation–reduction cycling. This unique property led to the demonstration of an electro-chemo-mechanical (ECM) actuator working at room temperature (Makagon *et al.*, 2020).

Thus, understanding the local structure of such composites may have direct and immediate implications for advancement of ECM materials and applications. For the V environment, conventional EXAFS analysis shows an underestimation of CNs. The possible explanations for the apparent inconsistency are that they have a heterogeneous environment with a multimodal distribution of bonds or a unimodal but strongly asymmetric environment. To investigate these effects, we performed a more in-depth pre-edge analysis to study the local symmetry of the above materials, as discussed in the rest of the article.

2. Experimental

Nanocomposite thin films were fabricated according to the previously published method (Makagon *et al.*, 2020). Namely, TiGDC20 (GDC20: 20% Gd-doped ceria) composites were deposited by a magnetron co-sputtering method on SiO_2 substrates with a 100 nm Al adhesion layer. Sample 1 was deposited from a Ti 2" metallic target and a GDC20 3" stoichiometric oxide target (Ar flow: 30 sccm, deposition pressure: 20 mTorr, DC power on Ti: 150 W, RF power on GDC20: 100 W, deposition time: 4 h, estimated thickness:1 µm). In Sample 2, the oxide target was replaced with a GDC20 alloy (Ar flow: 35 sccm, O_2 flow: 3 sccm, deposition pressure: 15 mTorr, DC power on Ti: 150 W, RF power on GDC20: 100 W, deposition time: 3 h, estimated thickness: 0.5 µm). VGDC20 samples were deposited under similar conditions to Sample 1 (DC power on V 2" metallic target: 100 W, RF power on GDC20: 100 W, deposition time: 4 h, estimated thickness: 200–500 nm). All samples were annealed under vacuum at 430°C for 4 h. Ti oxidation states and the overall grain morphology are expected to vary significantly between the samples. Ti (4966 eV) and V (5465 eV) *K*-edge X-ray absorption spectra of the TiGDC20 and VGDC20 thin films were measured at the QAS (7-BM) Beamline, National Synchrotron Light Source II (NSLS-II) at Brookhaven National Laboratory. X-ray absorption spectra were collected in fluorescence mode at grazing incidence. The experimental setup is shown in Fig. S1 of the supporting information. The raw XAFS data were analyzed utilizing the *Athena* and *Artemis* interfaces of the *Demeter* software package (Ravel & Newville, 2005). The spectra were energy-aligned, merged and normalized.

3. Results

3.1. The local structure of Ti in nanocomposites

For the Ti *K*-edge XANES spectra of Sample 1 and Sample 2, as shown in Fig. 1, the rising-edge positions resemble that of amorphous $BaTiO_3$ (Frenkel *et al.*, 2005), suggesting that the oxidation state of Ti in Sample 1 and Sample 2 is close to Ti^{4+}. As shown in Fig. S2, the oxidation state of Ti in Sample 1 is slightly lower than that in Sample 2. The inset in Fig. 1 shows the pre-edge feature A corresponding to the 1*s* to 3*d* transition in Ti. As demonstrated earlier (Farges *et al.*, 1997; Frenkel *et al.*, 2005), the intensities and energy positions of pre-edge peaks for Ti^{4+} species are well separated for different types of Ti local environment (Fig. 2). The energy position of Sample 1 and Sample 2 are aligned to compare with the components in the literature (Farges *et al.*, 1997; Frenkel *et al.*, 2005), which allows us to conclude that local environments of Ti in Sample 1 and Sample 2 are octahedral.

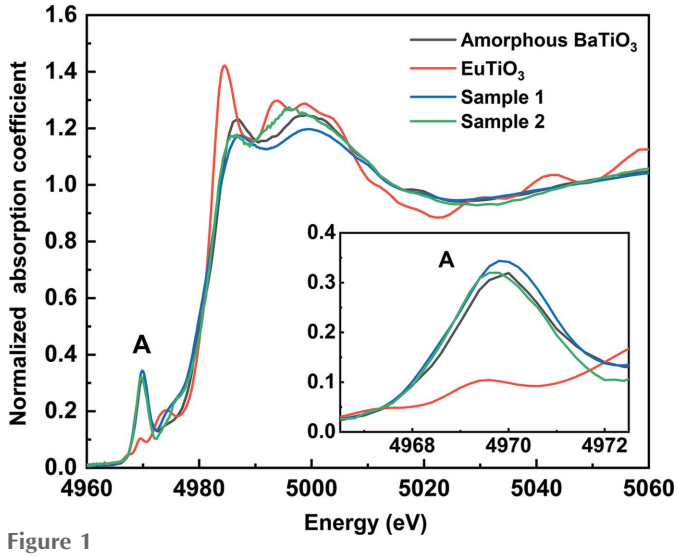

Figure 1
Ti *K*-edge XANES spectra of Sample 1, Sample 2, $EuTiO_3$ and amorphous $BaTiO_3$. The inset shows the zoomed-in pre-edge features (Peak A).

EXAFS analysis provides quantitative local structural information around Ti atoms. The CNs for the Ti—O bonds obtained by EXAFS fitting of Sample 1 and Sample 2 are 5.5 ± 1.0 and 6.1 ± 1.0, respectively, as shown in Table 1. Hence, the local environment of Ti estimated by EXAFS

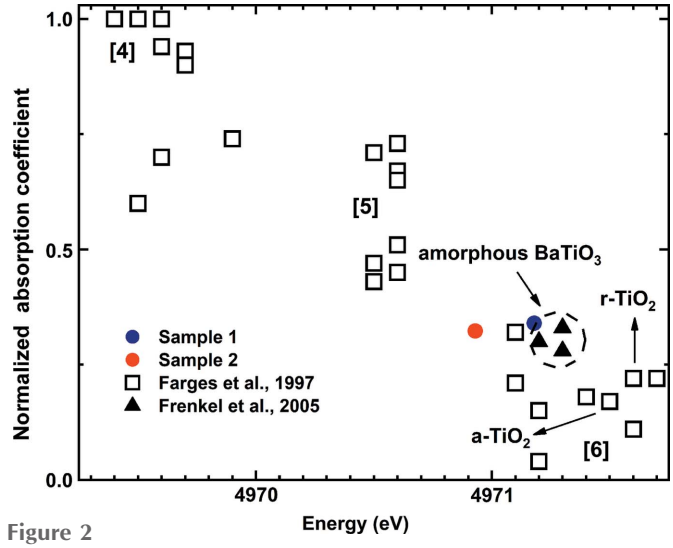

Figure 2
Normalized pre-edge height versus energy position for Ti *K*-pre-edge features in the model compound. There are three domains for fourfold, fivefold and sixfold coordinated Ti. Open squares (reproduced with permission) are from the literature (Farges *et al.*, 1997 & Frenkel *et al.*, 2005). Black triangles refer to the amorphous $BaTiO_3$ from the work by Frenkel *et al.* (2005). Colored symbols refer to the values obtained by the experimental XANES spectra in this work.

Table 1
Bond lengths (R) and disorder parameters (σ^2) of the two samples.

The σ^2 values for Ti—Ti and Ti—O contributions were constrained to be the same in the fit to lower the uncertainties.

	Path	CN	R (Å)	σ^2 (Å^2)
Sample 1	Ti—O	5.5 ± 1.0	1.91 ± 0.02	0.008 ± 0.003
	Ti—Ti	1.6 ± 0.8	3.01 ± 0.09	0.008
Sample 2	Ti—O	6.1 ± 1.0	1.91 ± 0.02	0.005 ± 0.003

analysis and taking into account the error bars is consistent with that of TiO_6 as also inferred from the XANES pre-edge features. The experimental EXAFS data and theoretical fits of Sample 1 and Sample 2 are shown in Fig. 3 in r-space. EXAFS analysis also indicates that that Sample 1 and Sample 2 differ with respect to the next-nearest neighbor (Ti–Ti) distribution. As shown in Fig. 3, EXAFS data for Sample 1 has a prominent second peak that corresponds to the Ti–Ti photoelectron path, which is not observed in Sample 2.

In addition to the CN and bond length, EXAFS analysis also provides information on the disorder in the TiO_6 octahedron. Related information which can be obtained by a more in-depth pre-edge analysis is on the off-center displacement d_i of the Ti atom from the center of the TiO_6 octahedron. We now discuss the relationship between the off-center displacement of the Ti atom to the disorder (σ^2) obtained by the EXAFS analysis in Sample 1 and Sample 2. The pre-edge area provides quantitative information on the off-center displacement. The area A_i of this pre-edge feature is proportional to the square of the off-center displacement (Ravel *et al.*, 1998; Ravel, 1995), as shown in equation (1),

$$A_i = \frac{\gamma_i}{3} d_i^2. \tag{1}$$

At 300 K, the experimentally measured constants γ_{BaTiO_3} and γ_{EuTiO_3} are 11.2 eV Å^{-2} and 13.6 eV Å^{-2}, respectively. We assume the value of γ_{TiO_x} to be the average of γ_{BaTiO_3} and γ_{EuTiO_3}: 12.4 eV Å^{-2}. $EuTiO_3$ is a centrosymmetric perovskite. The off-center displacement of $EuTiO_3$ is 0.103 Å at 300 K

Table 2
Ti atom off-center displacements obtained from *ex situ* experimental XANES spectra.

	Peak area	Off-center displacement (Å)
Ref. $EuTiO_3$	0.116	0.103
Sample 1	0.924	0.455
Sample 2	0.843	0.433

(Ravel *et al.*, 1998; Ravel, 1995), which refers to vibrational disorder within the TiO_6 octahedra. When calculating the off-center displacement of our samples, the peak area of $EuTiO_3$ is subtracted to correct for the thermal motion, as shown in equation (2),

$$A_{TiO_x} - A_{EuTiO_3} = \frac{\gamma_{TiO_x}}{3} d_{TiO_x}^2 - \frac{\gamma_{EuTiO_3}}{3} d_{EuTiO_3}^2. \tag{2}$$

The off-center displacements of Ti obtained for Sample 1 and Sample 2 are 0.455 Å and 0.433 Å, respectively, as shown in Table 2. According to the XANES and EXAFS analyses, Ti has a six-coordinated octahedral structure. Hence, the displacement change reflects that the Ti position changes from the octahedral center without any change in the overall local symmetry. Furthermore, the magnitude and direction of the off-center displacements of Ti atoms are the sources of the changes of individual Ti—O bond lengths (r), and must be related to the mean square relative displacement (σ^2), as shown in equation (3)

$$\sigma^2 = \left\langle (r - \mathbf{r})^2 \right\rangle. \tag{3}$$

We note however that a direct comparison of the displacements estimated by EXAFS from equation (3) and pre-edge analysis [equation (1)] is very complicated. In order to compare the two values, it is essential to take into account the correlation between the displacement of Ti and O atomic positions. Such analysis can be done, *e.g.* by molecular dynamics simulations or multi-technique Reverse Monte Carlo refinements (Noordhoek *et al.*, 2013).

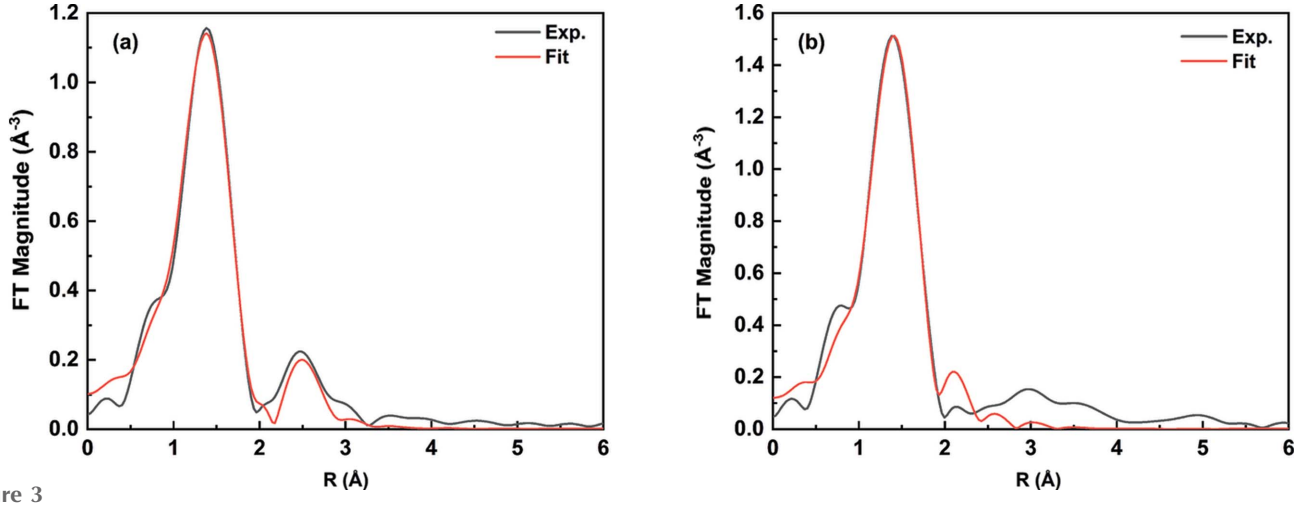

Figure 3
Fourier transform magnitudes of k^2-weighted EXAFS spectra of (*a*) Sample 1 and (*b*) Sample 2 and their theoretical fits. The k-range used in Fourier transforms was from 2 Å^{-1} to 9 Å^{-1}. The r-ranges used for fitting the data for Sample 1 and Sample 2 were 1–3.27 Å and 1–2 Å, respectively.

Table 3
EXAFS analysis results for VGDC20 sample.

Sample	Path	CN	R (Å)	σ^2 (Å^2)
VGDC20	V—O bond	2.0 ± 0.7	1.77 ± 0.03	0.004 ± 0.006

In the above analysis, the Ti samples have relatively ordered environment around the Ti atoms due to the overall octahedral symmetry. In these cases, the results obtained by EXAFS and pre-edge XANES analyses are consistent with each other. The above analysis also suggests that Ti with somewhat different oxidation state shares similar local coordination, which may be a hint to the ability of these composites to undergo rapid oxidation and reduction in the ECM effect (Makagon *et al.*, 2020).

3.2. The local structure of V in nanocomposites

We also employed V *K*-edge XANES and EXAFS data collected on the VGDC20 sample to obtain the valence states and CNs. As shown in Fig. 4, the rising edge position is between V_2O_4 and V_2O_5, indicating the average oxidation state of V in the sample is between V^{4+} and V^{5+}. The typical symmetry of tetravalent V can be square pyramidal (P_y) or octahedral (O_h). Pentavalent V may be present in several symmetries, such as T_d, O_h and P_y. Therefore, for the VGDC20 sample, the average CN of V is expected to be higher than 4 (the exact number should depend on the mixing fraction of multiple states with different symmetries). However, the CN obtained by EXAFS analysis is much smaller: 2.0 ± 0.7 (Table 3). The experimental spectra and theoretical fits in *r*-space are shown in Fig. 5.

To resolve the apparent discrepancy between EXAFS and XANES results for V compounds, we compare the two possible explanations: (1) the V environment is heterogeneous, containing a mixture of local structures and oxidation states, and hence, resulting in a multimodal distribution of V—O bond distances; or (2) V has the unimodal distribution of bonds but a strongly asymmetric environment. To discriminate between the two possibilities, we rely on the pre-edge analysis. Giuli *et al.* followed the procedure described by Farges *et al.* (1997), but found that intensity and energy position of pre-edge peaks for tetravalent and pentavalent V could not be well separated because each of them contains various symmetries (Giuli *et al.*, 2004; Levina *et al.*, 2014). Therefore, an interpretation of the pre-edge peak in terms of the distortion of V atoms from the inversion symmetry center should be made with extreme caution when more than one state of V can be present in the sample. If ignored, such heterogeneity will result in an erroneous assumption that there is an 'effective' V atom environment that such a method would characterize. Thus, the prevailing strategy is to use the pre-edge peak position and area for the task of speciation of structures and oxidation states of V in the sample. Only when a pure state is established, its analysis, based on the pre-edge peak intensity [equation (1)], can be undertaken, similar to that done above with Ti compounds.

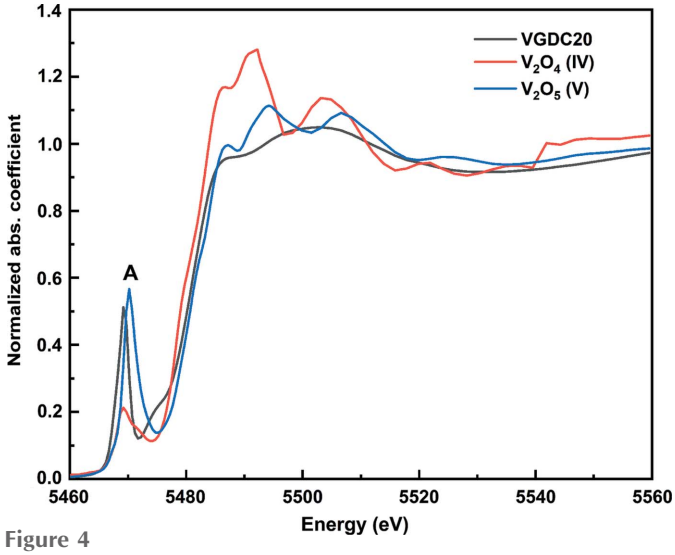

Figure 4
Normalized V *K*-edge XANES spectrum of VGDC20, as well as V_2O_4 and V_2O_5 standards.

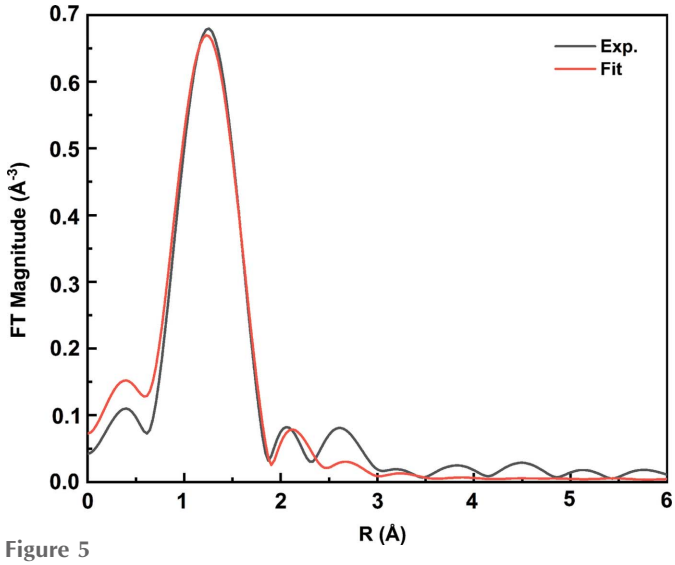

Figure 5
Experimental EXAFS data and theoretical fit for VGDC20. The EXAFS spectra were extracted in *k*-space, and Fourier transformation was carried out in the *k*-range 2–7.5 Å^{-1}. The range selected for fitting in *r*-space is 1–2.3 Å.

To evaluate the oxidation states and the symmetry of V oxides, we followed the procedure described by Chaurand *et al.* (2007). The evaluations of the oxidation states and the local symmetry of V are performed by employing the normalized pre-edge peak area and the pre-edge peak centroid energy, as shown in Fig. 6. Centroid energy is defined as the area-weighted average of the position in energy ($E - E_0$) of each component contributing to the pre-edge peak. E_0 is the maximum value of the first peak of the vanadium metal derivative spectrum, which marks the threshold or onset of photo-excitation of the 1*s* electron in vanadium metal (Bearden & Burr, 1967). The total pre-edge area was derived by calculating the sum of the integrated areas in each component in the vanadium pre-edge peak region. To correct for possible differences in experimental conditions, we assume

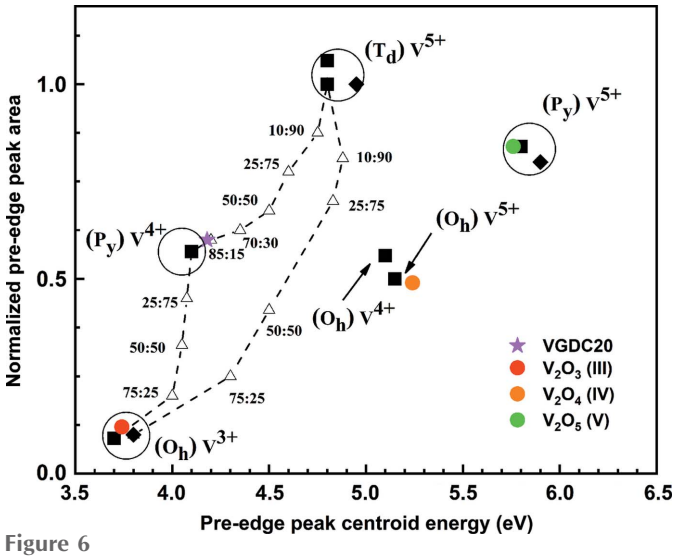

Figure 6
Plot of total pre-edge peak area [normalized according to Chaurand *et al.* (2007)] versus pre-edge peak centroid position. Black symbols, reproduced with permission, are from the work by Chaurand *et al.* (2007) and refer to the standard compounds (■) recorded at the ESRF synchrotron and compounds (◆) recorded at Elettra synchrotron. Open triangles from the work by Chaurand *et al.* (2007) refer to the mixtures of $(O_h)V^{3+}$ + $(P_y)V^{4+}$, $(P_y)V^{4+}$ + $(T_d)V^{5+}$ and $(O_h)V^{3+}$ + $(T_d)V^{5+}$. Colored symbols refer to the values obtained by the experimental XANES spectra collected at QAS, NSLS-II. The colored circles refer to the standard compounds: V_2O_3 (red), V_2O_4 (orange) and V_2O_5 (green), measured in this work. The pink star refers to the VGDC20 sample measured in this work.

that the normalized pre-edge peak area of V_2O_5 measured in this work is the same as the value in the literature (Chaurand *et al.*, 2007). The normalized pre-edge peak area in the VGDC20 sample is placed on the curve connecting the $V^{4+}(P_y)$ and V^{5+}(Td) states, indicating the coexistence of phases characterized by the T_d and P_y environments (Fig. 6). Due to the strong difference in the CNs and the symmetries between the T_d and P_y environments of V coexisting in this sample, the ensemble-average EXAFS data will be expected to have a non-symmetric distribution of nearest neighboring V—O bonds, explaining the underestimation of the V—O CN by conventional EXAFS analysis (Table 3).

4. Discussion and conclusions

In functional materials, the asymmetric bond length distribution poses the challenge to obtain reliable results by conventional EXAFS analysis. Furthermore, the low concentration of absorbing atoms, small size and experimental setup prevent us from collecting analyzable experimental EXAFS spectra. In this paper, we demonstrated the efficacy of pre-edge XANES analysis by comparing two types of materials, with symmetric and asymmetric local structures. This capability is important for studies of a large class of materials with local disorder such as nanoscale oxides and nanocomposites studied under realistic operating conditions, including recently investigated materials exhibiting electro-chemo-mechanical effects. For example, though there are no reports to date on the use of V-based nanocomposites in electro-chemo-mechanical actuation, the results shown in this work suggest that, by comparison with the Ti-based composites featuring the same locally tetrahedral environment while sustaining large bonding disorder, strongly non-symmetric distribution in V-based composites may be non-conducive for applications that require rapid oxidation–reduction.

The analyses presented has proven useful for two cases, where the environment around all absorbing atoms is either similar (a homogeneous case, as illustrated using Ti oxide nanocomposites) or changes across the sample (a heterogeneous case, shown using V oxide nanocomposites). In the former case, supervised machine learning-assisted analysis has been demonstrated as a powerful tool for structural refinement, well beyond the relatively limited result achieved by either EXAFS analysis or the pre-edge XANES fitting approach. In the latter case, special care is needed for machine learning analysis, due to the presence of multiple inequivalent environments. For that, deconvolution of the spectra using unsupervised approaches is required (Timoshenko & Frenkel, 2019).

5. Related literature

The following reference is cited in the supporting information: McKeown *et al.* (2002).

Acknowledgements

We gratefully acknowledge help of Dr Steven Ehrlich and Dr Lu Ma with beamline experiments at the QAS beamline of NSLS-II.

Funding information

AIF, JL, YL and PKR acknowledge support by National Science Foundation, Directorate for Mathematical and Physical Sciences (grant No. DMR-1911592). IL and AIF acknowledge the NSF-BSF program (grant No. 2018717). This research used beamline 7-BM (QAS) of the National Synchrotron Light Source II, a US DOE Office of Science User Facility operated for the DOE Office of Science by Brookhaven National Laboratory (contract No. DE-SC0012704).

References

Abrahams, S. C. (1978). *Mater. Res. Bull.* **13**, 1253–1258.
Ankudinov, A. L., Rehr, J. J., Low, J. J. & Bare, S. R. (2002). *J. Chem. Phys.* **116**, 1911–1919.
Bearden, J. A. & Burr, A. F. (1967). *Rev. Mod. Phys.* **39**, 125–142.
Billinge, S. J. & Levin, I. (2007). *Science*, **316**, 561–565.
Bingham, P. A., Hannant, O. M., Reeves-McLaren, N., Stennett, M. C. & Hand, R. J. (2014). *J. Non-Cryst. Solids*, **387**, 47–56.
Boubnov, A., Timoshenko, J., Wrasman, C. J., Hoffman, A. S., Cargnello, M., Frenkel, A. I. & Bare, S. R. (2020). *Radiat. Phys. Chem.* **175**, 108304.
Carbone, M. R., Topsakal, M., Lu, D. & Yoo, S. (2020). *Phys. Rev. Lett.* **124**, 156401.
Chaurand, P., Rose, J., Briois, V., Salome, M., Proux, O., Nassif, V., Olivi, L., Susini, J., Hazemann, J. L. & Bottero, J. Y. (2007). *J. Phys. Chem. B*, **111**, 5101–5110.

Chill, S. T., Anderson, R. M., Yancey, D. F., Frenkel, A. I., Crooks, R. M. & Henkelman, G. (2015). *ACS Nano*, **9**, 4036–4042.
Cicco, A., Minicucci, M., Principi, E., Witkowska, A., Rybicki, J. & Laskowski, R. (2002). *J. Phys. Condens. Matter*, **14**, 3365–3382.
Dalba, G., Fornasini, P., Grisenti, R. & Rocca, F. (2004). *J. Non-Cryst. Solids*, **345–346**, 7–15.
Dias, E. T., Gill, S. K., Liu, Y., Halstenberg, Ph., Dai, S., Huang, J., Mausz, J., Gakhar, R., Phillips, W. C., Mahurin, S., Pimblott, S. M., Wishart, J. F. & Frenkel, A. I. (2021). *J. Phys. Chem. Lett.* **12**, 157–164.
Farges, F., Brown, G. E. & Rehr, J. J. (1997). *Phys. Rev. B*, **56**, 1809–1819.
Farges, F., Lefrère, Y., Rossano, S., Berthereau, A., Calas, G. & Brown, G. E. (2004). *J. Non-Cryst. Solids*, **344**, 176–188.
Feldmann, C. (2003). *Adv. Funct. Mater.* **13**, 101–107.
Frenkel, A. I., Feldman, Y., Lyahovitskaya, V., Wachtel, E. & Lubomirsky, I. (2005). *Phys. Rev. B*, **71**, 024116.
Frenkel, A. I., Hills, C. W. & Nuzzo, R. G. (2001). *J. Phys. Chem. B*, **105**, 12689–12703.
Giuli, G., Paris, E., Mungall, J., Romano, C. & Dingwell, D. (2004). *Am. Mineral.* **89**, 1640–1646.
Grunes, L. A. (1983). *Phys. Rev. B*, **27**, 2111–2131.
Gurman, S. J. & McGreevy, R. L. (1990). *J. Phys. Condens. Matter*, **2**, 9463–9473.
Joly, Y. (2001). *Phys. Rev. B*, **63**, 125120.
Levina, A., McLeod, A. I. & Lay, P. A. (2014). *Chem. Eur. J.* **20**, 12056–12060.
Liu, Y., Marcella, N., Timoshenko, J., Halder, A., Yang, B., Kolipaka, L., Pellin, M., Seifert, S., Vajda, S., Liu, P. & Frenkel, A. I. (2019). *J. Chem. Phys.* **151**, 164201.
Makagon, E., Wachtel, E., Houben, L., Cohen, S. R., Li, Y., Li, J., Frenkel, A. I. & Lubomirsky, I. (2020). *Adv. Funct. Mater.* **31**, 2006712.
Mazzone, G., Rivalta, I., Russo, N. & Sicilia, E. (2008). *J. Phys. Chem. C*, **112**, 6073–6081.
McGreevy, R. L. & Pusztai, L. (1988). *Mol. Simul.* **1**, 359–367.
McGreevy, R. L. & Pusztai, L. (1990). *Proc. Math. Phys. Eng. Sci.* **430**, 241–261.
McKeown, D. A., Muller, I. S., Matlack, K. S. & Pegg, I. L. (2002). *J. Non-Cryst. Solids*, **298**, 160–175.
Noordhoek, M. J., Krayzman, V., Chernatynskiy, A., Phillpot, S. R. & Levin, I. (2013). *Appl. Phys. Lett.* **103**, 022909.
Penner-Hahn, J. E. (1999). *Coord. Chem. Rev.* **190–192**, 1101–1123.
Prasai, B., Wilson, A. R., Wiley, B. J., Ren, Y. & Petkov, V. (2015). *Nanoscale*, **7**, 17902–17922.
Ravel, B. & Newville, M. (2005). *J. Synchrotron Rad.* **12**, 537–541.
Ravel, B., Stern, E. A., Vedrinskii, R. I. & Kraizman, V. (1998). *Ferroelectrics*, **206**, 407–430.
Ravel, B. (1995). PhD thesis. University of Washington, USA.
Rehr, J. J. & Albers, R. C. (2000). *Rev. Mod. Phys.* **72**, 621–654.
Rehr, J. J., Albers, R. C. & Zabinsky, S. I. (1992). *Phys. Rev. Lett.* **69**, 3397–3400.
Roscioni, O. M., Zonias, N., Price, S. W. T., Russell, A. E., Comaschi, T. & Skylaris, C. K. (2011). *Phys. Rev. B*, **83**, 115409.
Sayers, D. E., Lytle, F. W. & Stern, E. A. (1969). *Adv.X-ray Anal.* **13**, 248–271.
Sayers, D. E., Stern, E. A. & Lytle, F. W. (1971). *Phys. Rev. Lett.* **27**, 1204–1207.
Srivastava, U. C. & Nigam, H. L. (1973). *Coord. Chem. Rev.* **9**, 275–310.
Timoshenko, J., Duan, Z., Henkelman, G., Crooks, R. M. & Frenkel, A. I. (2019). *Annu. Rev. Anal. Chem.* **12**, 501–522.
Timoshenko, J. & Frenkel, A. I. (2017). *Catal. Today*, **280**, 274–282.
Timoshenko, J. & Frenkel, A. I. (2019). *ACS Catal.* **9**, 10192–10211.
Torrisi, S. B., Carbone, M. R., Rohr, B. A., Montoya, J. H., Ha, Y., Yano, J., Suram, S. K. & Hung, L. (2020). *Npj Comput. Mater.* **6**, 109.
Ueda, S. (2013). *J. Electron Spectrosc. Relat. Phenom.* **190**, 235–241.
Vaccari, M., Aquilanti, G., Pascarelli, S. & Mathon, O. (2009). *J. Phys. Condens. Matter*, **21**, 145403.
Vinson, J., Rehr, J. J., Kas, J. J. & Shirley, E. L. (2011). *Phys. Rev. B*, **83**, 115106.
Wang, L., Zhang, Z. & Han, X. (2013). *NPG Asia Mater.* **5**, e40.
Wende, H. (2004). *Rep. Prog. Phys.* **67**, 2105–2181.
Yamamoto, T. (2008). *X-ray Spectrom.* **37**, 572–584.
Yancey, D. F., Chill, S. T., Zhang, L., Frenkel, A. I., Henkelman, G. & Crooks, R. M. (2013). *Chem. Sci.* **4**, 2912–2921.
Yevick, A. & Frenkel, A. I. (2010). *Phys. Rev. B*, **81**, 115451.